On the Roles of Precipitation and Entrainment in Stratocumulus Transitions between Mesoscale States

Hoffmann, Fabian; Glassmeier, Franziska; Yamaguchi, Takanobu; Feingold, Graham

DOI
10.1175/JAS-D-22-0268.1

Publication date
2023

Document Version
Final published version

Published in
Journal of the Atmospheric Sciences

On the Roles of Precipitation and Entrainment in Stratocumulus Transitions between Mesoscale States

FABIAN HOFFMANN,[a] FRANZISKA GLASSMEIER,[b] TAKANOBU YAMAGUCHI,[c,d] AND GRAHAM FEINGOLD[d]

[a] *Meteorologisches Institut, Ludwig-Maximilans-Universität München, Munich, Germany*
[b] *Delft University of Technology, Delft, Netherlands*
[c] *Cooperative Institute for Research in Environmental Sciences, University of Colorado Boulder, Boulder, Colorado*
[d] *Chemical Sciences Laboratory, NOAA/Earth System Research Laboratories, Boulder, Colorado*

(Manuscript received 30 December 2022, in final form 7 July 2023, accepted 14 September 2023)

ABSTRACT: Stratocumulus occur in closed- or open-cell states, which tend to be associated with high or low cloud cover and the absence or presence of precipitation, respectively. Thus, the transition between these states has substantial implications for the role of this cloud type in Earth's radiation budget. In this study, we analyze transitions between these states using an ensemble of 127 large-eddy simulations, covering a wide range of conditions. Our analysis is focused on the behavior of these clouds in a cloud fraction (f_c) scene albedo (A) phase space, which has been shown in previous studies to be a useful framework for interpreting system behavior. For the transition from closed to open cells, we find that precipitation creates narrower clouds and scavenges cloud droplets for all f_c. However, precipitation decreases the cloud depth for $f_c > 0.8$ only, causing a rapid decrease in A. For $f_c < 0.8$, the cloud depth actually increases due to mesoscale organization of the cloud field. As the cloud deepening balances the effects of cloud droplet scavenging in terms of influence on A, changes in A are determined by the decreasing f_c only, causing a linear decrease in A for $f_c < 0.8$. For the transition from open to closed cells, we find that longwave radiative cooling drives the cloud development, with cloud widening dominating for $f_c < 0.5$. For $f_c > 0.5$, clouds begin to deepen gradually due to the decreasing efficiency of lateral expansion. The smooth switch between cloud widening and deepening leads to a more gentle change in A compared to the transitions under precipitating conditions.

SIGNIFICANCE STATEMENT: By reflecting a substantial fraction of solar shortwave radiation back to space, shallow clouds constitute a major cooling agent in Earth's radiation budget. To constrain this effect, a profound understanding of cloud cover and cloud albedo is necessary. In this study, we analyze the processes that drive the variability in these cloud properties in stratocumulus clouds, a very common cloud type covering approximately 20% of the globe. For these clouds, we show that changes from low to high or high to low cloud cover are different due to the underlying cloud micro- and macrophysics, elucidating this crucial aspect of aerosol–cloud–climate interactions.

KEYWORDS: Cloud cover; Cloud microphysics; Cloud radiative effects; Cloud parameterizations; Cloud resolving models; Aerosol-cloud interaction

1. Introduction

The planetary albedo is strongly affected by the presence of clouds that, in their net effect, increase the amount of shortwave radiation reflected back to space, constituting a major cooling agent in the Earth radiation budget (e.g., Loeb et al. 2018). Shallow boundary layer clouds, such as shallow cumulus and stratocumulus, primarily affect the climate system in this way due to their proximity to the surface, limiting potential counteracting effects via the emission of longwave radiation. While the ability of individual clouds to reflect shortwave radiation is primarily determined by their liquid water content and number of cloud droplets (e.g., Twomey 1974, 1977), the horizontal cloud cover is another important factor determining the radiative effect of clouds in the climate system (e.g., Albrecht 1989). Canonical examples for systematic cloud cover changes in shallow boundary layer clouds are the transition of closed- to open-cell or open- to closed-cell stratocumulus (e.g., Wang and Feingold 2009; Yamaguchi et al. 2015), as well as the transition from stratocumulus to shallow cumulus (e.g., Sandu and Stevens 2011; Goren et al. 2019).

In this study, we will focus on the transition of closed- to open-cell and open- to closed-cell stratocumulus. These stratocumulus mesoscale states are linked to the specific organization of the up- and downdraft regions in the cells in which this cloud type is organized (e.g., Helfand and Kalnay 1983). In closed-cell stratocumulus, broad updrafts dominate the center of the cells, causing approximately full cloud cover, while narrow bands of downdrafts are found on the edges of the cell, which are associated with a small reduction in cloud cover due to the entrainment of free-tropospheric air primarily taking place in these regions (Gerber et al. 2005). If these clouds start to precipitate, cold pools caused by evaporating raindrops drive the updrafts to the edges of the cells, where narrower and deeper clouds form on their tops, and downdrafts dominate the cell center. Following the direct dissipation of the cloud by precipitation, the

Denotes content that is immediately available upon publication as open access.

Corresponding author: Fabian Hoffmann, fa.hoffmann@lmu.de

DOI: 10.1175/JAS-D-22-0268.1

subsequent stabilization of the subcloud layer limits the transport of moisture to the cloud layer such that the cloud cover of open-cell stratocumulus often reaches only a few tens of percent (Savic-Jovcic and Stevens 2008; Wang and Feingold 2009). Thus, this transition of closed- to open-cell stratocumulus is primarily caused by the initiation of precipitation, while the transition of open- to closed-cell stratocumulus requires not only the absence of precipitation but also the buildup of liquid water and hence radiative cooling to drive the underlying convection (Feingold et al. 2015). Beyond the scope of this study are transitions caused by changes in boundary layer depth or surface fluxes, as well as wind shear (e.g., Wood 2012).

The scene albedo A is often used to approximate the effect of clouds on the planetary albedo, and it is frequently expressed as

$$A = A_s(1 - f_c) + A_c f_c, \tag{1}$$

where A_s is the surface albedo, A_c is the cloud albedo, and f_c is the cloud fraction (Schneider and Dickinson 1976). The cloud albedo A_c can be determined by a simple two-stream approximation following Bohren (1987) as

$$A_c = \frac{\tau_c}{\gamma + \tau_c}, \tag{2}$$

where $\gamma \approx 13.3$ is a parameter that depends on the degree of forward scattering and τ_c is the cloud optical thickness:

$$\tau_c = \alpha N_c^{1/3} \mathrm{LWP}_c^{5/6}, \tag{3}$$

with N_c being the cloud droplet concentration, $\mathrm{LWP}_c = \int_{z_b}^{z_t} q_c dz$ being the liquid water path, i.e., the liquid water content q_c integrated from cloud base z_b to cloud top z_t, and $\alpha \approx 0.2\ \mathrm{m}^{8/3}\ \mathrm{kg}^{-5/6}$, a temperature- and pressure-dependent parameter (e.g., Stephens 1978).

For the aforementioned examples of closed- and open-cell stratocumulus, but also stratocumulus transitioning to shallow cumulus, the relationship between A and f_c has been found to obey a relatively universal functional relationship that was first documented by Bender et al. (2011), who analyzed satellite imagery of marine stratocumulus in selected subtropical regions. Engström et al. (2015) expanded their analysis by sampling all marine clouds between 60°N and 60°S over 12 years. The relationship discovered by Engström et al. (2015) has been described as exponential, superlinear, or by a power law and has been confirmed in various modeling studies and satellite observations subsequently (Feingold et al. 2016, 2017; McCoy et al. 2017; Rampal and Davies 2020). For instance, Feingold et al. (2017) showed that the shape of this relationship can be explained by the deepening of clouds while they widen, causing a higher LWP_c and hence a larger τ_c, A_c, and A for increasing f_c. Moreover, Feingold et al. (2016) showed a systematic increase in N_c with f_c, which can also explain the increase in A with f_c. Thus, the degree to which N_c and LWP modulate A_c with respect to f_c remains uncertain.

To understand the transitions between stratocumulus mesoscale states and the associated changes in A as a function of f_c further, this study compiles 127 large-eddy simulations (LESs) of stratocumulus-topped boundary layers. This ensemble enables us to understand the transitions of stratocumulus from a dynamical systems perspective, rather than individual case studies. This study will begin with a short summary of the simulations (section 2), followed by their analysis (section 3), beginning with a general overview of their behavior before precipitating, and nonprecipitating cases are analyzed individually. The study is concluded in section 4.

2. Setup, production, and evaluation of LES ensembles

The simulations for this study were conducted with the System for Atmospheric Modeling (SAM) (Khairoutdinov and Randall 2003), which uses the LES approach to solve the anelastic Navier–Stokes equations and transport equations for total water and liquid water static energy. Cloud microphysics are simulated with a bin-emulating, two-moment bulk scheme, covering droplet activation, condensation, and precipitation processes (Feingold et al. 1998).

The simulations are loosely based on the nocturnal, drizzling, marine stratocumulus case by Ackerman et al. (2009), as further detailed in our previous LES ensemble studies (Feingold et al. 2016; Glassmeier et al. 2019, 2021; Hoffmann et al. 2020; Feingold et al. 2022). In short, the simulation domain is set to $48 \times 48\ \mathrm{km}^2$ in the horizontal direction and 2.5 km in the vertical. The horizontal extent is chosen to allow for adequate mesoscale organization (e.g., Kazil et al. 2017). The grid spacing is set to 200 m horizontally and 10 m vertically. While the grid spacing can be considered coarse for an individual simulation, it is a necessity to produce the large number of ensemble simulations for this study. While finer grid spacings tend to increase LWP_c and f_c, the applied anisotropic grid spacing can mitigate this dependency (e.g., Mellado et al. 2018), and the general sensitivities analyzed in this study are expected to be reliable. The simulation time step is 1 s, and simulations are run for 12 h. We disregard the first 2 h as model spinup. Precipitation is inhibited for the first hour. As the simulated cases are nocturnal, shortwave radiation has been neglected, while longwave emission is represented using the Rapid Radiative Transfer Model (RRTM) (Iacono et al. 2000). The sea surface temperature is set to 293.34 K, and the subsidence is determined from a fixed large-scale divergence of $3.75 \times 10^{-6}\ \mathrm{s}^{-1}$ (Ackerman et al. 2009). A surface aerosol source of $70\ \mathrm{cm}^{-2}\ \mathrm{s}^{-1}$ (Yamaguchi et al. 2017) is added to represent various processes that result in an increase in aerosol (sea spray, new particle formation, advection), which is necessary to counter the runaway aerosol scavenging by precipitation. The simulations feature interactive surface sensible and latent heat fluxes that are determined using Monin–Obukhov similarity theory, which have been used in only one of our previous ensemble studies so far (Feingold et al. 2022). Note that these surface fluxes are somewhat smaller than those prescribed in our other ensemble studies with constant surface fluxes (Fig. 1) but within the range of previous measurements and simulations of stratocumulus (e.g., Large and Pond 1982; Hourston 1992; Kazil et al. 2014; Feingold et al. 2015).

For initial conditions, we systematically varied five variables that are traditionally used to characterize a stratocumulus-topped boundary layer in a mixed-layer framework and one variable to determine cloud microphysics to initialize the simulations: the mixed-layer depth ($500\ \mathrm{m} \leq z_i \leq 1300\ \mathrm{m}$), mixed-layer

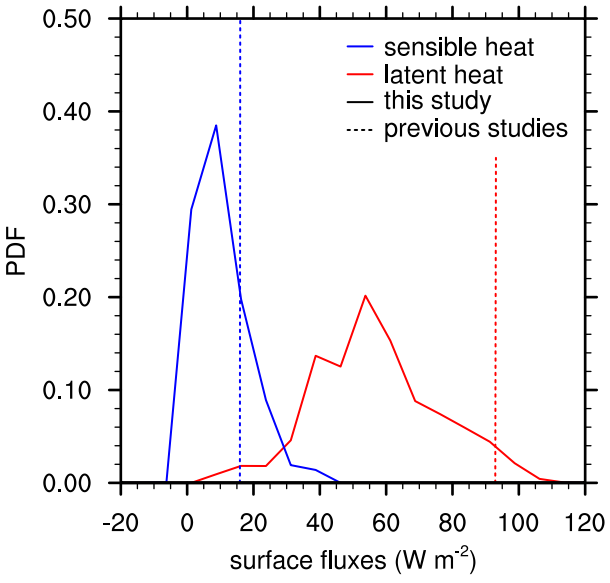

FIG. 1. Probability density distributions (PDFs) of sensible (blue lines) and latent (red lines) surface heat fluxes from this (continuous lines) and our previous (dashed lines) LES ensemble studies. Note that our previous studies assumed constant surface fluxes.

liquid water potential temperature ($284\ \mathrm{K} \le \theta_l \le 294\ \mathrm{K}$), mixed-layer total water mixing ratio ($6.5\ \mathrm{g\ kg^{-1}} \le q_t \le 10.5\ \mathrm{g\ kg^{-1}}$), liquid water potential temperature difference between mixed-layer and free troposphere ($6\ \mathrm{K} \le \Delta\theta_l \le 10\ \mathrm{K}$), total water mixing ratio difference between mixed-layer and free troposphere ($-10\ \mathrm{g\ kg^{-1}} \le \Delta q_t \le -6\ \mathrm{g\ kg^{-1}}$), and the mixed-layer aerosol concentration ($30\ \mathrm{cm^{-3}} \le N_a \le 500\ \mathrm{cm^{-3}}$). This variable space was examined using Latin-hypercube sampling to prevent correlations between these variables (e.g., Feingold et al. 2016). From all initialized cases, 127 simulations produced a cloud. These will be analyzed below.

From our simulations, we determine A using (1) with (2) and (3) for each column of the simulation domain individually to avoid any biases due to the inhomogeneity of the cloud field that may arise if A_c was determined from the domain-averaged LWP_c and N_c (Glenn et al. 2020). We further assume $A_s = 0.08$, which is typical for oceans (e.g., Jin et al. 2004). In the following, the subscript c indicates that a variable (e.g., f_c, τ_c, LWP_c, or N_c) is evaluated only from cloudy columns in the simulation domain. To consider a column as cloudy, we apply a threshold of $\tau_c > 5$ to exclude optically thin clouds. This value ensures that the analysis is focused on the most active regions of the clouds that drive their transitions by the production of precipitation or substantial longwave radiative cooling. However, we do not want to understate the importance of optically thin clouds on A. A sensitivity study on the τ_c threshold will be presented below.

3. Results

In this section, we will first lay out basic properties of the entire ensemble and describe how we separated the ensemble members into precipitating and nonprecipitating cases. These subensembles will be addressed in more detail in the subsequent subsections.

a. Overview

Figure 2a shows the trajectories of all analyzed simulations in the aforementioned A–f_c phase space. Based on details provided later, precipitating and nonprecipitating cases are colored in different shades of blue and red, respectively, while cases that do not fall into any of these categories are indicated by a thin black line. A thick black line shows the satellite reference from Engström et al. (2015), which will be used as a reference below. Generally, all simulated cases follow that reference, especially its curvature, albeit at somewhat higher A. As we will see below, this overestimation is partially due to the high threshold for τ_c used for analyzing the model output. Note further that the precipitating cases move predominantly from high to low f_c, while the nonprecipitating cases move in the opposite direction (cf. Figs. 4b and 6b). This motion in the A–f_c phase space is primarily due to the transition between open and closed cells or closed and open cells, respectively, as analyzed in more depth below.

To distinguish between precipitating and nonprecipitating cases, we assessed the cloud-base rain rate R_{cb} (Figs. 2b,c). Simulations with continuous $R_{\mathrm{cb}} > 1\ \mathrm{mm\ day^{-1}}$ during the analyzed time will be considered as precipitating (blue lines, 19 simulations), while simulations with continuous $R_{\mathrm{cb}} < 1\ \mathrm{mm\ day^{-1}}$ during the analyzed time will be considered nonprecipitating (red lines, 107 simulations). Only one simulation (thin black line) does not fall into these categories and will be disregarded in the subsequent analysis. A threshold for R_{cb} on the order of $1\ \mathrm{mm\ day^{-1}}$ is often applied to distinguish between heavy and weakly precipitating stratocumulus (cf. Wood 2012) and is indicative of the steady states in N_c that stratocumulus assume due to the competing effects of the surface source and precipitation scavenging (Baker and Charlson 1990).

Figures 2d and 2e show joint frequency distributions of all trajectories separated into precipitating and nonprecipitating cases, while Fig. 2f shows the joint frequency distribution for all cases. Only the analyzed time steps are considered. The corresponding average $\overline{A}$ values are shown as *continuous* blue, red, and orange lines, respectively. As a reminder, these averages are always determined using a threshold of $\tau_c = 5$ to discriminate between cloudy and noncloudy regions unless otherwise noted. Long- and short-dashed lines show $\overline{A}$ for lower τ_c thresholds of 2 and 1. Unsurprisingly, smaller τ_c thresholds lead to a smaller $\overline{A}$, while maintaining the general shape of $\overline{A}$. Thus, the following analysis to understand the shape of $\overline{A}$ is not substantially dependent on the applied threshold of τ_c.

What does $\overline{A}$ show? For the nonprecipitating cases, which transition toward larger f_c, $\overline{A}$ exhibits a superlinear increase for all f_c (Fig. 2e). This behavior is very similar to the satellite reference by Engström et al. (2015) (thick black line), while overestimating A for all f_c slightly, which might be due to the higher τ_c threshold used for this study, as argued above. For the precipitating cases, which transition from high to low f_c, one sees a rapid decrease in $\overline{A}$ for $f_c > 0.8$, followed by an almost linear and more gradual decrease for smaller f_c (Fig. 2d). Again, the Engström et al. (2015) reference is exceeded, but now more

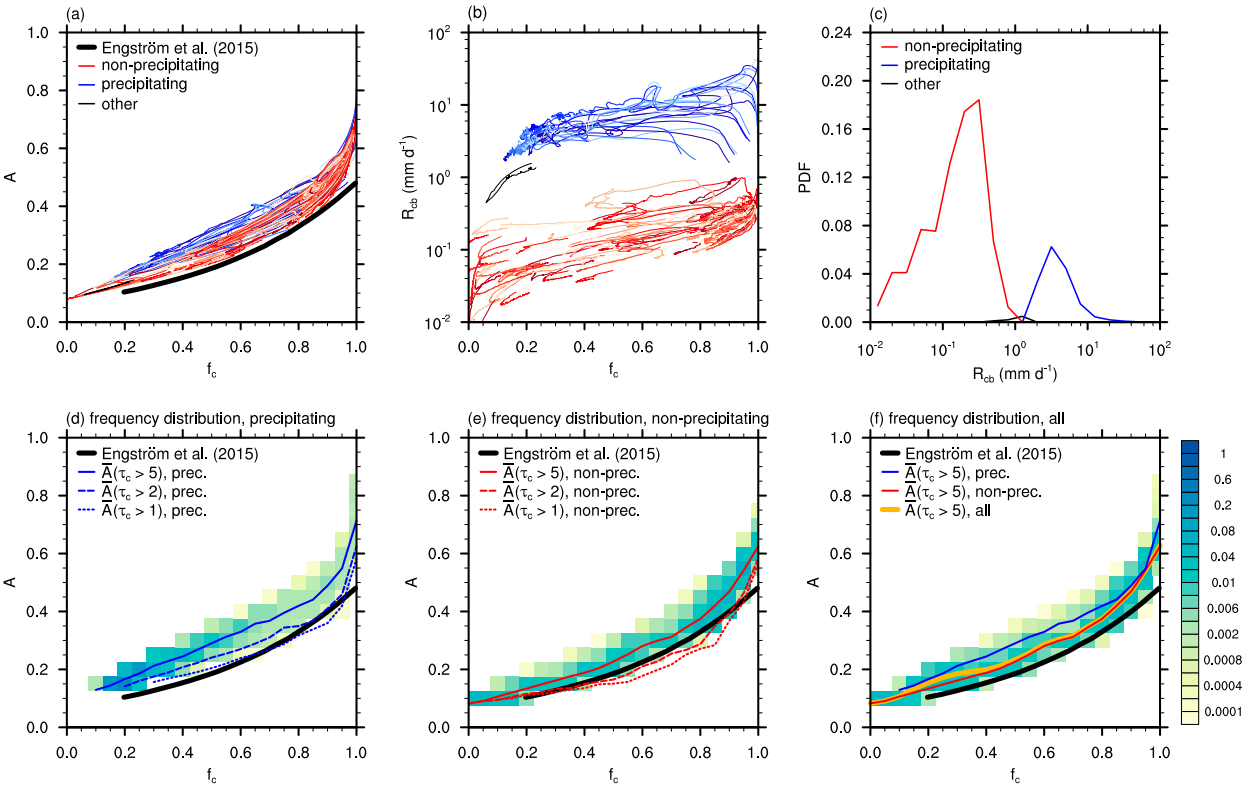

FIG. 2. (a) All simulations as trajectories in an A–f_c phase space, with blue lines indicating precipitating cases and red lines indicating nonprecipitating cases. (The differently shaded blue and red lines are an aid to distinguishing the trajectories and have no further meaning.) A thin black line shows the trajectory that does not fall in the precipitating or nonprecipitating categories applied here. A thick black line shows the reference by Engström et al. (2015). (b) The same simulations in an R_{cb}–f_c phase space and (c) PDFs of R_{cb}. (d)–(f) Complement to (a) with corresponding joint frequency distributions for the cases classified as precipitating or nonprecipitating, as well as all cases combined. The respective blue, red, and orange lines show the average $\overline{A}$ for $\tau_c = 5$ (continuous lines), 2 (long-dashed lines), and 1 (short-dashed lines). Note that the threshold $\tau_c = 5$ is used throughout the study.

distinctly. In addition to the τ_c-threshold bias, this is due to the generally higher LWP_c in the precipitating cases (cf. Figs. 3b and 5b below). Most importantly, however, the shape of the precipitating $\overline{A}$ differs substantially from the Engström et al. (2015) reference and hence the nonprecipitating cases. Note that these differences in $\overline{A}$ for precipitating and nonprecipitating stratocumulus would be indistinguishable in the reference by Engström et al. (2015), which includes all marine clouds in the sampled regions.

In any case, the different shapes of $\overline{A}$ for the precipitating and nonprecipitating cases indicate a hysteretic system, where different processes dominate the transitions from high to low (precipitating cases) and from low to high f_c (nonprecipitating). Understanding the underlying processes will be the main subject of the next two subsections.

b. *Precipitating cases*

We will focus on the precipitating cases first, starting with a general overview of A_c, LWP_c, N_c, and $\mathrm{RWP}_c/\mathrm{LWP}_c$ in the A–f_c phase space introduced above (Fig. 3). In this and all the following depictions of the A–f_c phase space, each pixel represents the average of all precipitating (or nonprecipitating) trajectories passing through its boundaries, using all analyzed time steps. Here, RWP_c is the vertically integrated rainwater path, analogous to LWP_c but restricted to droplets with radii > 25 μm, a threshold which is often applied to discriminate between cloud and raindrops (e.g., Khairoutdinov and Kogan 2000). For a given f_c, A_c must increase to cause a larger A per definition (1), while A_c also shows generally larger values at higher f_c (Fig. 3a). These changes are determined by changes in LWP_c and N_c, as expected from (2). Indeed, LWP_c generally increases with A for a given f_c (Fig. 3b). The distribution of N_c (Fig. 3c) is mostly determined by precipitation scavenging, reducing N_c by collision and coalescence, as indicated by the largely anticorrelated $\mathrm{RWP}_c/\mathrm{LWP}_c$ (population Pearson correlation coefficient of -0.65), which marks the most active precipitation in this region of the phase space (Fig. 3d). Overall, N_c tends to be higher for larger f_c, which is due to the less active precipitation in this part of the phase space, in agreement with Feingold et al. (2016).

Figures 4a–c show the temporal changes in A, f_c, and A_c, which are connected via

$$\frac{dA}{dt} = (A_c - A_s)\frac{df_c}{dt} + \frac{dA_c}{dt}f_c, \tag{4}$$

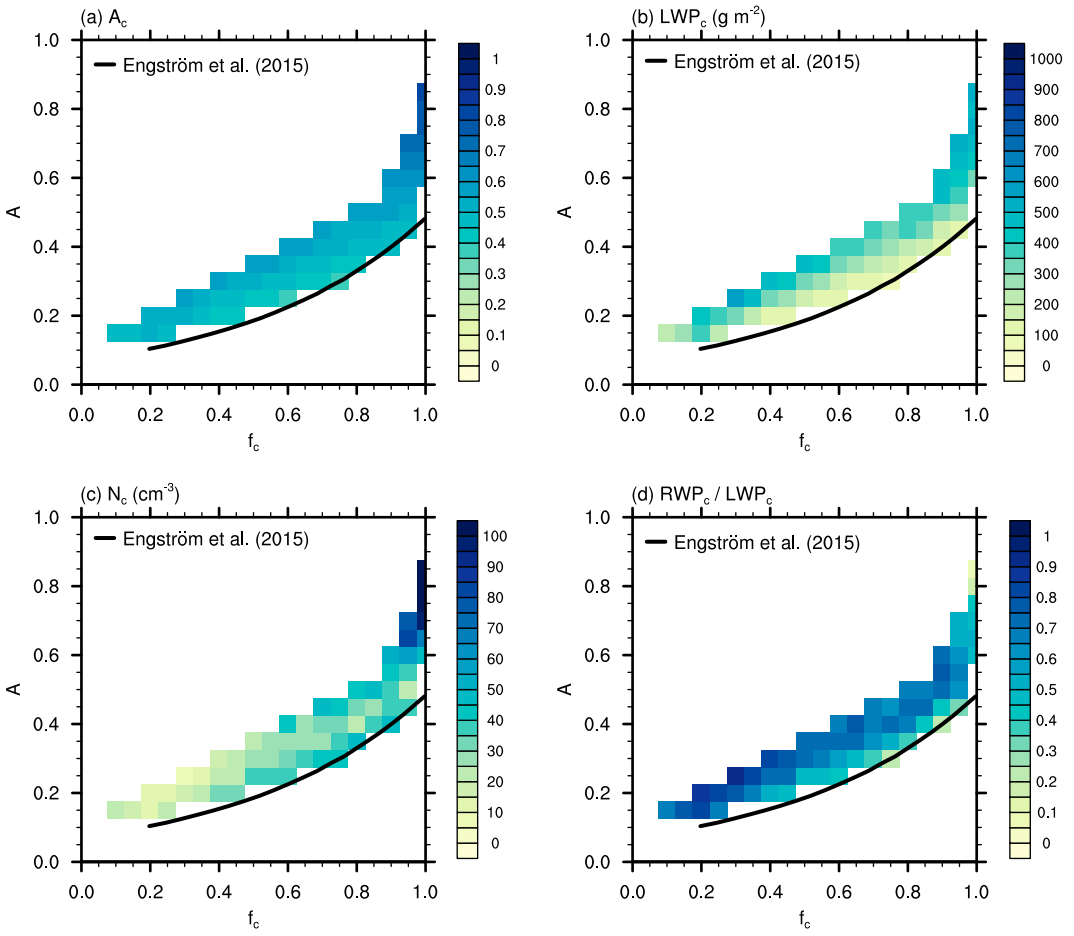

FIG. 3. For the precipitating cases, (a) A_c, (b) LWP_c, (c) N_c, and (d) $\mathrm{RWP}_c/\mathrm{LWP}_c$ are displayed in an A–f_c phase space. The black line shows the reference by Engström et al. (2015).

derived from differentiating (1) and assuming $dA_s/dt = 0$. The temporal derivatives are determined using finite differences after applying a running average of 20 min to each trajectory to filter small-scale fluctuations. The dA/dt is negative throughout most of the phase space, with the strongest negative tendencies for $f_c \approx 1$ that approach zero for $f_c \approx 0.1$ (Fig. 4a). These changes are primarily determined by df_c/dt (Fig. 4b), which shows a similar distribution, although with slightly less negative values for $f_c \approx 1$. The onset of precipitation is most apparent in dA_c/dt, which shows the strongest negative tendencies for $f_c > 0.8$ (Fig. 4c) due to losses in LWP_c and N_c. However, $dA_c/dt \approx 0$ for $f_c < 0.8$. While this behavior is necessary to cause the aforementioned linear change in $\overline{A}$ for $f_c < 0.8$, it is surprising because precipitation and hence its potential effects on A_c do not disappear for $f_c < 0.8$ (cf. Figs. 2b and 3d).

To understand this, dA_c/dt is expanded as

$$\frac{dA_c}{dt} = \gamma \frac{A_c^2}{\tau_c}\left[\frac{1}{3}\frac{d\ln(N_c)}{dt} + \frac{5}{6}\frac{d\ln(\mathrm{LWP}_c)}{dt}\right], \tag{5}$$

using (2) and (3), with $\gamma A_c^2/\tau_c \approx 0.2$ for $5 < \tau_c < 30$, typical for stratocumulus (e.g., Pawlowska et al. 2000). Figures 4d and 4g show the total $d\ln(\mathrm{LWP}_c)/dt$ and $d\ln(N_c)/dt$; the corresponding changes due to surface precipitation and precipitation scavenging only are depicted in Figs. 4e and 4h, respectively. Indeed, precipitation reduces LWP_c and N_c for all f_c, with the strongest reduction in N_c for $f_c > 0.8$, which explains the rapid reduction in $\overline{A}$ in this part of the phase space. However, the total $d\ln(\mathrm{LWP}_c)/dt$ is positive for $f_c < 0.8$. This corresponds to the aforementioned change in the mesoscale organization of the cloud field, where shallow closed-cell stratocumulus transition into deeper and narrower cloud bands (open-cell stratocumulus) due to convergence zones created by cold pools formed by evaporating precipitation (Savic-Jovcic and Stevens 2008; Wang and Feingold 2009). The commensurate change in the cloud aspect ratio, determined as the quotient of average cloud width to average cloud depth, confirms this (Fig. 4f). Combining the effects of cloud deepening [$d\ln(\mathrm{LWP}_c)/dt > 0$, Fig. 4d] and precipitation scavenging [$d\ln(N_c)/dt < 0$, Fig. 4g] yields the net-zero change in A_c for $f_c < 0.8$ (Fig. 4c). While the cancellation of these two effects might be accidental here, the tendency of precipitation-induced cold pools to enable deeper clouds, and hence buffer the negative effects of precipitation scavenging of N_c on A_c, has been noted earlier (e.g., Stevens and Feingold 2009).

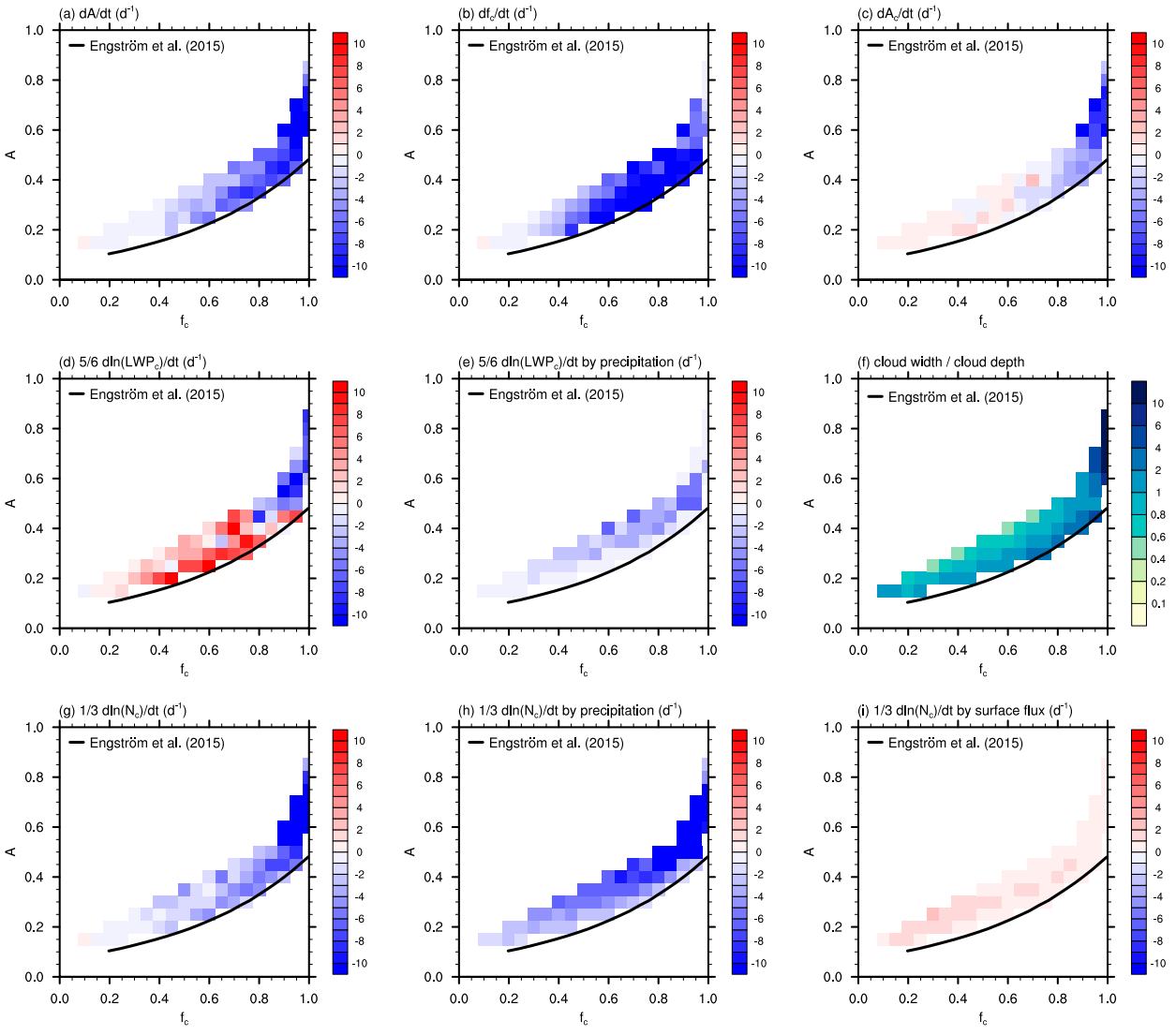

FIG. 4. For the precipitating cases, the temporal change in (a) A, (b) f_c, (c) A_c, (d) LWP$_c$, (e) LWP$_c$ by precipitation, (g) N_c, (h) N_c by precipitation, and (i) N_c by surface sources is presented. (f) The cloud aspect ratio is shown. The black line indicates the reference by Engström et al. (2015).

Finally, it is interesting to see that the low N_c steady state predicted by Baker and Charlson (1990), in which the surface source for N_c (Fig. 4i) matches the losses through precipitation (Fig. 4h), is reproduced at $f_c \approx 0.1$. Combined with the vanishing tendencies for LWP$_c$ (Fig. 4d), this indicates that $f_c \approx 0.1$ can constitute a steady state in the examined phase space for this set of simulations.

c. *Nonprecipitating cases*

The less understood transition from open- to closed-cell stratocumulus in the absence of precipitation is introduced in Fig. 5, showing the distribution of A_c, LWP$_c$, N_c, and RWP$_c$/LWP$_c$ in the A–f_c phase space. As in the precipitating cases in Fig. 3a, A_c exhibits larger values for higher A (Fig. 5a). In contrast to the precipitating cases, N_c shows no clear pattern in the A–f_c phase space (Fig. 5c), while LWP$_c$ increases substantially with A and f_c (Fig. 5b). Per definition, there is no precipitation in the nonprecipitating cases (Fig. 5d).

Figures 6a–c show the temporal derivatives of A, f_c, and A_c, respectively. For dA/dt and df_c/dt, we see a distinct band of positive values for all f_c, representing the transition from open to closed cells in the absence of precipitation. Based on (4), we see that dA/dt is mainly driven by df_c/dt, while the contribution from dA_c/dt to dA/dt is mostly negligible. Only for $f_c > 0.5$ does dA_c/dt exhibit a region of distinctly positive values, which are due to a temporal increase in LWP$_c$ (Fig. 6d), while there are no substantial changes in N_c (Fig. 6e). Nonetheless, this slight increase in LWP$_c$ is essential to explain the superlinear increase in $\overline{A}$ discussed above. Figure 6f shows the buoyancy integral ratio, a decoupling index developed by Turton and Nicholls (1987), which is based on the ratio of buoyancy destruction below cloud base to the buoyancy

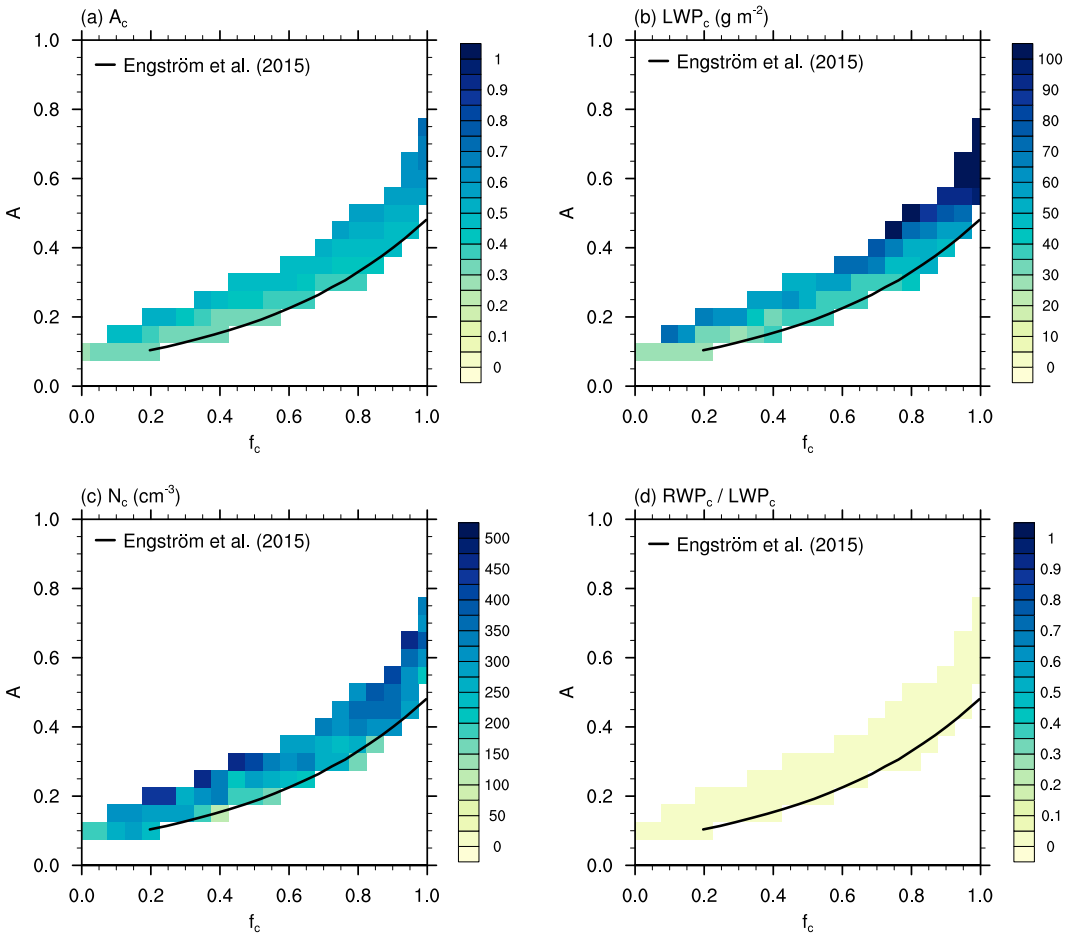

FIG. 5. For the nonprecipitating cases, (a) A_c, (b) LWP_c, (c) N_c, and (d) RWP_c/LWP_c are displayed in an A–f_c phase space. The black line shows the reference by Engström et al. (2015).

production in the entire boundary layer [see (14) in Bretherton and Wyant 1997]. A value above 0.15 indicates a decoupled boundary layer. As the entire phase space is below this threshold, the nonprecipitating cases presented in this subsection can be considered well mixed, which is a necessary prerequisite for the mixed-layer analysis presented below.

We focus on the changes in LWP_c along the positive bands of dA/dt and df_c/dt first. The zero or slightly negative tendencies below the positive bands will be briefly addressed by the end of this subsection.

To analyze the behavior of LWP_c more comprehensively, Fig. 7a shows $d\mathrm{LWP}_c/dt$ directly from LES (thick black line) and mixed-layer model (MLM) tendencies diagnosed from the LESs using the approach presented in Hoffmann et al. (2020), which allows one to expand $d\mathrm{LWP}_c/dt$ into contributions by cloud-top motion (blue line), cloud-top entrainment (green line), precipitation (cyan line), surface fluxes (purple line), and radiation (red line). For this, we determine the divergence of the corresponding fluxes of the total water mixing ratio and liquid water potential temperature across the LES mixed layer to determine the influence of precipitation, surface fluxes, and radiation. The effect of cloud-top motion is determined from the temporal change in cloud-top height. Cloud-top entrainment is diagnosed using the approach by Yamaguchi and Randall (2008, appendix E), which aims to minimize storage of total water mixing ratio and liquid water potential temperature in the inversion layer. A new term, which was not considered in Hoffmann et al. (2020), is the change in liquid water due to the horizontal development of the cloud layer, i.e., lateral entrainment (yellow line). For Fig. 7a, this term is determined as the difference between the sum of all the previously mentioned MLM tendencies (dashed black line) and the LES tendency (thick black line) as a residuum. This term will be discussed more deeply below, including direct estimates that are not based on determining a residuum. Note that all quantities are determined for regions with $df_c/dt > 0$ only to avoid the aforementioned regions that do not exhibit a transition from open to closed cells. Further note that the trajectories providing the data for these plots are binned in f_c space, and then averaged.

The deepening of the boundary layer enables higher cloud tops and hence larger LWP_c (cloud-top motion) (blue line in Fig. 7a), while the simultaneous mixing with free-tropospheric air evaporates the cloud and decreases LWP_c (cloud-top entrainment) (green line). Together, these two terms represent

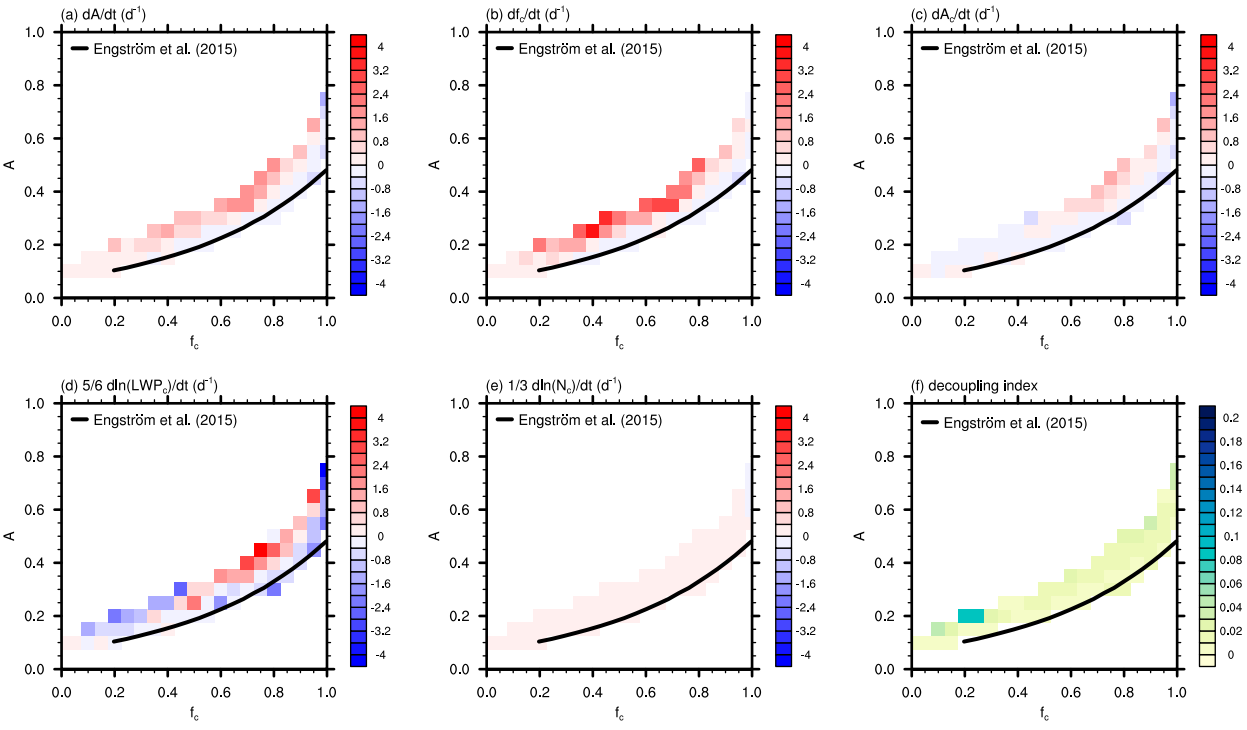

FIG. 6. For the nonprecipitating cases, the temporal change in (a) A, (b) f_c, (c) A_c, (d) LWP$_c$, (e) N_c, and (f) a decoupling index is presented. The black line shows the reference by Engström et al. (2015).

the net effect of cloud-top entrainment on LWP$_c$, which is slightly negative and becomes more negative for larger f_c. This dependency on f_c is expected because cloud-top entrainment requires the preconditioning of free-tropospheric air by cloud evaporation (Yamaguchi and Randall 2012), a process that naturally scales with f_c. Consequently, a larger f_c will accelerate cloud-top motion and cloud-top entrainment. The surface fluxes (purple line) are slightly negative for all f_c, indicating that the influx of sensible heat, causing evaporation, exceeds the influx of water vapor, causing condensation, and thus leads to a lower LWP$_c$. Longwave radiative cooling (red line) constitutes the largest positive LWP$_c$ tendency and increases with f_c. Stronger radiative cooling with f_c is expected due to the larger cloud amount contributing to the emission of longwave radiation. Combining all these MLM tendencies results in a positive impact on LWP$_c$ for all f_c (dashed black line). While this MLM estimate agrees with the LES (thick black line) for $f_c = 1$, it overestimates the LES tendency for all $f_c < 1$.

We will show that the difference between the sum of all MLM tendencies and the LES tendency is due to lateral cloud development, which is traditionally not considered in MLMs but becomes a necessity for $f_c < 1$ (yellow line in Fig. 7a). This thought is developed further in Fig. 7b, where df_c/dt is determined from the LESs directly (black line), a theoretical estimate (blue line), and the lateral entrainment tendency of Fig. 7a (yellow line). For the last approach, we assume that

$$\left.\frac{d\mathrm{LWP}_c}{dt}\right|_{\mathrm{lat.entr.}} = -\frac{df_c}{dt}(\mathrm{LWP}_c + \delta\mathrm{LWP}), \qquad (6)$$

where $d\mathrm{LWP}_c/dt|_{\mathrm{lat.entr.}}$ is the lateral entrainment tendency from Fig. 7a, while LWP$_c$ and δLWP are shown in Fig. 7c. Here, $\delta\mathrm{LWP} = \int_{z_b}^{z_t}(q_s - q_v)dz$ is the vertically integrated liquid water deficit in the region between the clouds, where q_v is the water vapor density and q_s is the corresponding saturation value. Note that (6) is an approximation of the underlying physics, considering only the amount of liquid water necessary to saturate a fraction of the environment (δLWP) and to adjust it to liquid water of the rest of the cloud deck (LWP$_c$). In that sense, (6) represents the limiting case in which there is sufficient kinetic energy to sustain lateral expansion. Alternatively, it might be possible that the lateral transport is limited by the available kinetic energy, making it slower than predicted by (6) (e.g., MacVean and Mason 1990). However, Fig. 7b shows good agreement between (6) (yellow line) and the LES reference (black line), which supports the aforementioned limiting case driven by sufficient kinetic energy. This indicates that the excess in LWP$_c$ production predicted by the MLM, and here mostly due to longwave radiative cooling, is used for the lateral expansion. Only the decreasing efficiency of df_c/dt for $f_c > 0.5$ enables cloud deepening and hence larger LWP$_c$. Last, this analysis indicates that the excess in LWP$_c$ production predicted by the MLM is not due to inherent uncertainties in determining MLM tendencies from LES data (e.g., McMichael et al. 2019) but is indeed the signal of a physical process.

What determines the efficiency of df_c/dt? The df_c/dt is approximately zero for $f_c = 0$ and 1 and exhibits a maximum in

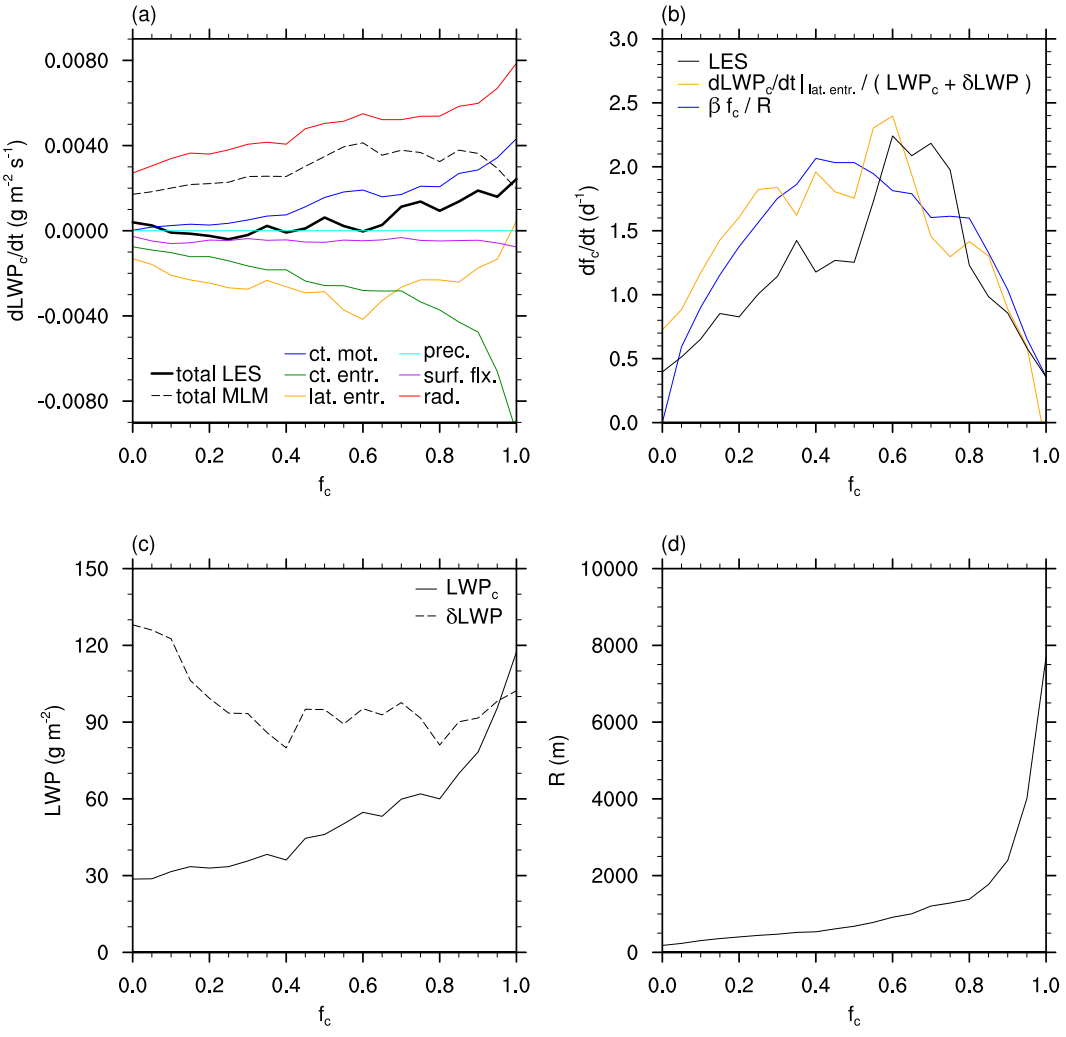

FIG. 7. (a) The temporal change in LWP_c determined using MLM equations [cloud-top motion (blue line), cloud-top entrainment (green line), precipitation (cyan line), surface fluxes (purple line), longwave radiation (red line), and the total tendency (dashed black line)], the total LWP_c tendency from the LES (thick black line), and the difference between the total LWP_c tendencies of LES and MLM termed lateral entrainment (yellow line). (b) The temporal change in f_c determined from LES (black line), the lateral entrainment rate (yellow line), and a theoretical estimate (blue line). (c) The LWP_c (continuous black line) and the liquid water deficit δLWP (dashed black line). (d) The average cloud radius R. Quantities in (c) and (d) are derived from LESs.

between. To analyze this behavior, we determine df_c/dt from the continuity equation

$$\frac{\partial f_c}{\partial t} - E + \frac{\partial (f_c w_c)}{\partial z} = 0, \tag{7}$$

which is the basis of many lateral entrainment parameterizations [cf. (6) in de Rooy et al. 2013]. Here, E is the net entrainment rate describing the horizontal cloud development, and $\partial f_c w_c/\partial z$ accounts for the vertical cloud development, with w_c being the in-cloud vertical velocity. While one commonly uses a vertical profile of f_c in (7), we restrict our analysis to the maximum of the f_c profile, which corresponds to the two-dimensional cloud cover assessed in this study. Usually, the maximum of the f_c profile coincides with a (local) maximum of the $f_c w_c$ profile, and hence, the derivative $\partial(f_c w_c)/\partial z$ can be neglected in this study (cf. Stevens et al. 2001; Siebesma et al. 2003). Thus, we get

$$\frac{\partial f_c}{\partial t} = E \approx \beta \frac{f_c}{R}, \tag{8}$$

which uses a simple estimate for E based on an entraining plume (Morton et al. 1956), with R being the plume (or cloud) radius (Fig. 7d). Following (10) in de Rooy et al. (2013), $R = 2a_c/p_c$, the ratio of cloud area a_c to cloud perimeter p_c. The terms a_c and p_c are determined as bulk quantities of the two-dimensional projection of the entire cloud field, i.e., regions with $\tau_c > 5$. Individual cloud elements are not considered explicitly, which is a simplification that is frequently applied in parameterizations of the entrainment process (e.g., Yanai et al. 1973).

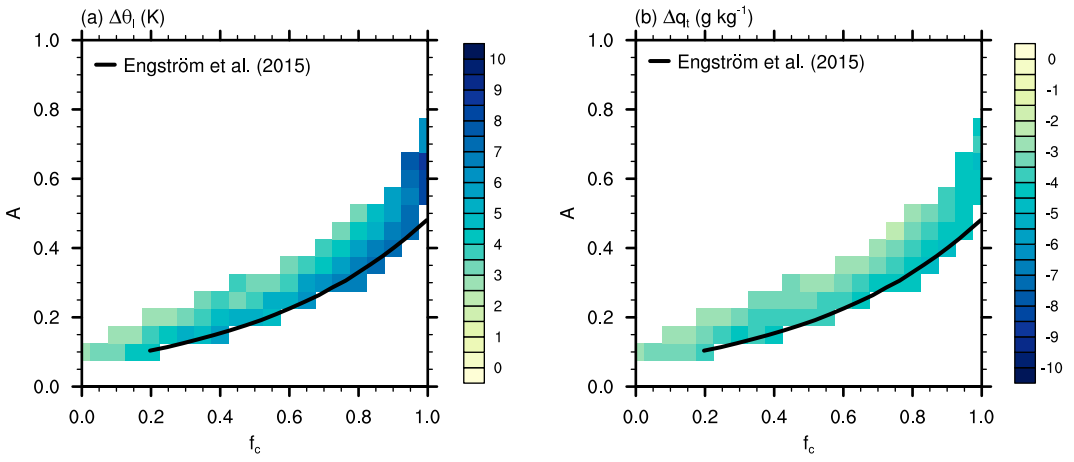

FIG. 8. For the nonprecipitating cases, differences between free-tropospheric and boundary layer thermodynamic quantities are shown for (a) $\Delta\theta_1$ and (b) Δq_t; the black line shows the reference by Engström et al. (2015).

Thus, R needs to be interpreted as an average quantity of the cloud field rather than describing the radius of an individual cloud. With $\beta \approx 2800$ m day^{-1}, the estimate of $\partial f_c/\partial t$ matches the general behavior of the LESs well (Fig. 7b). Based on (8), we understand that for $f_c = 0$, df_c/dt is zero because there are no clouds from which new clouds can be generated. For $f_c = 1$, df_c/dt approaches zero because of the increasing R, indicating a decreasing cloud perimeter to cloud area ratio that reduces the transport of liquid water to the lateral environment. This interplay naturally favors an intermediate f_c for the most efficient transport of liquid water. Overall, this indicates that cloud geometry, introduced by f_c and R, plays an important role in determining the temporal development of cloud fields (cf. Feingold et al. 2017; Rampal and Davies 2020).

Finally, we return to the regions of zero or slightly negative tendencies below the positive bands of dA/dt and df_c/dt in Figs. 6a and 6b, in which the stratocumulus are not transitioning. Figure 8a shows that these regions are characterized by a larger $\Delta\theta_1$. The associated stability limits entrainment and hence the vertical cloud development, resulting in the lower LWP$_c$ shown in Fig. 5b. While one might expect a commensurate increase in the horizontal cloud development when updrafts are blocked at a strong inversion and deflected laterally, $df_c/dt \approx 0$ in this region of the phase space. As discussed above, radiative cooling is the primary driver for the transition of nonprecipitating stratocumulus from an open- to a closed-cell state, and the influence of radiative cooling is proportional to the cloud amount. Thus, the comparably low LWP$_c$ limits radiative cooling and hence the potential for a substantial increase in f_c. While this halts the transition of the cloud deck (cf. Feingold et al. 2015), individual stratocumulus may be sustained for longer periods of time (e.g., McMichael et al. 2019). In contrast to $\Delta\theta_1$, Δq_t varies only slightly in the analyzed phase space (Fig. 8b). A drier free troposphere could increase the evaporation of LWP$_c$ due to the entrainment of drier air. However, a drier free troposphere might also increase longwave radiative cooling of the cloud layer by decreasing the downward radiative flux reaching the cloud layer (e.g., Held and Soden 2000), which could cause a positive LWP$_c$ tendency. All in all, this last analysis indicates that the transitioning of stratocumulus is not only determined by the cloud layer intrinsically but is also dependent on external factors such as the lower tropospheric stability. This finding amends the work by Wood and Bretherton (2006), who showed that a higher lower tropospheric stability correlates well with high f_c: While a higher lower tropospheric stability might indeed stabilize already high f_c by decreasing the influence of entrainment, it might also prevent a system from reaching that high f_c state by preventing the necessary buildup of liquid water.

4. Summary

Stratocumulus clouds exist in two distinct states commonly referred to as open cell and closed cell, which are associated with lower and almost full cloud cover (f_c), respectively, and substantial changes in the scene albedo (A). Thus, the transition between these states has important implications for the Earth radiation budget and hence the climate system. In this study, we used 127 large-eddy simulations (LESs) with bin-emulating cloud microphysics to understand the transitions in marine stratocumulus in a much wider phase space than possible with individual case studies (Feingold et al. 2016). In this study, transitions are primarily driven by the presence or absence of precipitation. Thus, the LESs are separated into precipitating (cloud-base rain rate $R_{cb} > 1$ mm day^{-1}) and nonprecipitating cases ($R_{cb} < 1$ mm day^{-1}). Beyond the scope of this study, but similarly important, are transitions caused by changes in boundary layer depth or surface fluxes, as well as wind shear (e.g., Wood 2012).

Based on previous satellite observations (Engström et al. 2015), we analyzed transitions in a reduced phase space employing the aforementioned A and f_c as its dimensions. In this framework, observations and simulations populate a remarkably narrow region, with generally low A at low f_c and large A at large f_c, despite the wide range of initial and boundary conditions in our stratocumulus simulations.

Our study showed that the transitions follow different trajectories in the A–f_c phase space depending on the degree of precipitation. During their transition from closed to open cells, precipitating stratocumulus generally approach low f_c from high f_c, while nonprecipitating stratocumulus do the opposite during their transition from open to closed cells. The average trajectory of the precipitating cases exhibits a slightly higher A than the nonprecipitating cases and shows a strong initial decrease in A for $f_c > 0.8$, followed by a scale break and a more gradual and almost linear decrease in A for $f_c < 0.8$. The nonprecipitating cases show a continuous increase in A for all f_c, without any scale breaks. This hysteretic behavior, previously emphasized by Feingold et al. (2015), is not apparent in the large statistical composite satellite reference by Engström et al. (2015), which is based on *all* marine clouds between 60°N and 60°S. In fact, the satellite reference is very similar to the average trajectory of the nonprecipitating stratocumulus cases, which might indicate that precipitating stratocumulus constitute a minority in the satellite data (e.g., Leon et al. 2008).

For the precipitating cases, we found that the reduction in f_c through precipitation (cloud narrowing) is the main driver for the transition toward the open-cell state. To understand the concurrent changes in A, we analyzed the in-cloud liquid water path LWP_c and cloud droplet concentration N_c. Precipitation losses in LWP_c and N_c drive the initial reduction in A for $f_c > 0.8$. For $f_c < 0.8$, precipitation is still active and scavenges N_c, but LWP_c increases due to the mesoscale organization of the cloud field which enables deeper clouds (Savic-Jovcic and Stevens 2008). Due to the opposite impacts of N_c scavenging and cloud deepening on the cloud albedo, the net effect of these two processes on A is negligible for $f_c < 0.8$, which causes A to change linearly with f_c for $f_c < 0.8$.

For the nonprecipitating cases, we confirmed that the emission of longwave radiative cooling is the main driver for the transition toward larger f_c (cloud widening) and higher LWP_c (cloud deepening) (cf. Feingold et al. 2015). Our analysis showed that the cloud evolution is restricted to cloud widening for $f_c < 0.5$. For $f_c > 0.5$, however, cloud widening is successively replaced by cloud deepening until $f_c = 1$ is reached. The continuous change from cloud widening to cloud deepening explains the steady increase in the cloud albedo and hence the steady superlinear increase in A with f_c. We argued that this change in growth mode is caused by the decreasing efficiency of lateral entrainment at larger f_c, where increasing cloud radii make the detrainment of liquid water to the environment less efficient. Overall, changes in N_c are negligible for the nonprecipitating cases.

Understanding the transitions of stratocumulus and the underlying micro- and macrophysical processes is essential to constrain the role of clouds in the climate system (e.g., Boucher et al. 2013). Given the high sensitivity of A on f_c demonstrated above, this study emphasizes the necessity to extend our understanding of aerosol–cloud–climate interactions beyond the well-established effect of N_c on cloud reflectivity (Twomey 1974, 1977) and to include the more complex adjustments of LWP_c (e.g., Glassmeier et al. 2021) and f_c (e.g., Yamaguchi et al. 2017). To achieve this requires bridging the process-level and system-wide understanding of clouds attempted in this study, as well as an assessment of the frequency of occurrence of different stratocumulus mesoscale states and their transitions.

Acknowledgments. FH appreciates support from the Emmy Noether Program of the German Research Foundation (DFG) under Grant HO 6588/1-1. FG acknowledges support from The Branco Weiss Fellowship—Society in Science, administered by ETH Zurich, and from an NWO Veni grant. GF acknowledges funding from NOAA's ERB program (NOAA CPO Climate and CI 03-01-07-001). Marat Khairoutdinov graciously provided the SAM model.

Data availability statement. The data that support the findings of this study are available from the corresponding author upon request.

REFERENCES

Ackerman, A. S., and Coauthors, 2009: Large-eddy simulations of a drizzling, stratocumulus-topped marine boundary layer. *Mon. Wea. Rev.*, **137**, 1083–1110, https://doi.org/10.1175/2008MWR2582.1.

Albrecht, B. A., 1989: Aerosols, cloud microphysics, and fractional cloudiness. *Science*, **245**, 1227–1230, https://doi.org/10.1126/science.245.4923.1227.

Baker, M. B., and R. J. Charlson, 1990: Bistability of CCN concentrations and thermodynamics in the cloud-topped boundary layer. *Nature*, **345**, 142–145, https://doi.org/10.1038/345142a0.

Bender, F. A.-M., R. J. Charlson, A. M. L. Ekman, and L. V. Leahy, 2011: Quantification of monthly mean regional-scale albedo of marine stratiform clouds in satellite observations and GCMs. *J. Appl. Meteor. Climatol.*, **50**, 2139–2148, https://doi.org/10.1175/JAMC-D-11-049.1.

Bohren, C. F., 1987: Multiple scattering of light and some of its observable consequences. *Amer. J. Phys.*, **55**, 524–533, https://doi.org/10.1119/1.15109.

Boucher, O., and Coauthors, 2013: Clouds and aerosols. *Climate Change 2013: The Physical Science Basis*, T. F. Stocker et al., Eds., Cambridge University Press, 571–657.

Bretherton, C. S., and M. C. Wyant, 1997: Moisture transport, lower-tropospheric stability, and decoupling of cloud-topped boundary layers. *J. Atmos. Sci.*, **54**, 148–167, https://doi.org/10.1175/1520-0469(1997)054<0148:MTLTSA>2.0.CO;2.

de Rooy, W. C., and Coauthors, 2013: Entrainment and detrainment in cumulus convection: An overview. *Quart. J. Roy. Meteor. Soc.*, **139**, 1–19, https://doi.org/10.1002/qj.1959.

Engström, A., F. A.-M. Bender, R. J. Charlson, and R. Wood, 2015: The nonlinear relationship between albedo and cloud fraction on near-global, monthly mean scale in observations and in the CMIP5 model ensemble. *Geophys. Res. Lett.*, **42**, 9571–9578, https://doi.org/10.1002/2015GL066275.

Feingold, G., R. L. Walko, B. Stevens, and W. R. Cotton, 1998: Simulations of marine stratocumulus using a new microphysical parameterization scheme. *Atmos. Res.*, **47–48**, 505–528, https://doi.org/10.1016/S0169-8095(98)00058-1.

——, I. Koren, T. Yamaguchi, and J. Kazil, 2015: On the reversibility of transitions between closed and open cellular convection. *Atmos. Chem. Phys.*, **15**, 7351–7367, https://doi.org/10.5194/acp-15-7351-2015.

——, A. McComiskey, T. Yamaguchi, J. S. Johnson, K. S. Carslaw, and K. S. Schmidt, 2016: New approaches to quantifying aerosol influence on the cloud radiative effect. *Proc. Natl.*

Acad. Sci. USA, **113**, 5812–5819, https://doi.org/10.1073/pnas.1514035112.

——, J. Balsells, F. Glassmeier, T. Yamaguchi, J. Kazil, and A. McComiskey, 2017: Analysis of albedo versus cloud fraction relationships in liquid water clouds using heuristic models and large eddy simulation. *J. Geophys. Res. Atmos.*, **122**, 7086–7102, https://doi.org/10.1002/2017JD026467.

——, T. Goren, and T. Yamaguchi, 2022: Quantifying albedo susceptibility biases in shallow clouds. *Atmos. Chem. Phys.*, **22**, 3303–3319, https://doi.org/10.5194/acp-22-3303-2022.

Gerber, H., G. Frick, S. P. Malinowski, J.-L. Brenguier, and F. Burnet, 2005: Holes and entrainment in stratocumulus. *J. Atmos. Sci.*, **62**, 443–459, https://doi.org/10.1175/JAS-3399.1.

Glassmeier, F., F. Hoffmann, J. S. Johnson, T. Yamaguchi, K. S. Carslaw, and G. Feingold, 2019: An emulator approach to stratocumulus susceptibility. *Atmos. Chem. Phys.*, **19**, 10 191–10 203, https://doi.org/10.5194/acp-19-10191-2019.

——, ——, ——, ——, ——, and ——, 2021: Aerosol-cloud-climate cooling overestimated by ship-track data. *Science*, **371**, 485–489, https://doi.org/10.1126/science.abd3980.

Glenn, I. B., G. Feingold, J. J. Gristey, and T. Yamaguchi, 2020: Quantification of the radiative effect of aerosol–cloud interactions in shallow continental cumulus clouds. *J. Atmos. Sci.*, **77**, 2905–2920, https://doi.org/10.1175/JAS-D-19-0269.1.

Goren, T., J. Kazil, F. Hoffmann, T. Yamaguchi, and G. Feingold, 2019: Anthropogenic air pollution delays marine stratocumulus breakup to open cells. *Geophys. Res. Lett.*, **46**, 14 135–14 144, https://doi.org/10.1029/2019GL085412.

Held, I. M., and B. J. Soden, 2000: Water vapor feedback and global warming. *Annu. Rev. Energy Environ.*, **25**, 441–475, https://doi.org/10.1146/annurev.energy.25.1.441.

Helfand, H. M., and E. Kalnay, 1983: A model to determine open or closed cellular convection. *J. Atmos. Sci.*, **40**, 631–650, https://doi.org/10.1175/1520-0469(1983)040<0631:AMTDOO>2.0.CO;2.

Hoffmann, F., F. Glassmeier, T. Yamaguchi, and G. Feingold, 2020: Liquid water path steady states in stratocumulus: Insights from process-level emulation and mixed-layer theory. *J. Atmos. Sci.*, **77**, 2203–2215, https://doi.org/10.1175/JAS-D-19-0241.1.

Hourston, R. A. S., 1992: Variability of North Pacific Ocean surface sensible and latent heat fluxes. M.S. thesis, Dept. of Atmospheric Science, The University of British Columbia, 151 pp.

Iacono, M. J., E. J. Mlawer, S. A. Clough, and J.-J. Morcrette, 2000: Impact of an improved longwave radiation model, RRTM, on the energy budget and thermodynamic properties of the NCAR Community Climate Model, CCM3. *J. Geophys. Res.*, **105**, 14 873–14 890, https://doi.org/10.1029/2000JD900091.

Jin, Z., T. P. Charlock, W. L. Smith Jr., and K. Rutledge, 2004: A parameterization of ocean surface albedo. *Geophys. Res. Lett.*, **31**, L22301, https://doi.org/10.1029/2004GL021180.

Kazil, J., G. Feingold, H. Wang, and T. Yamaguchi, 2014: On the interaction between marine boundary layer cellular cloudiness and surface heat fluxes. *Atmos. Chem. Phys.*, **14**, 61–79, https://doi.org/10.5194/acp-14-61-2014.

——, T. Yamaguchi, and G. Feingold, 2017: Mesoscale organization, entrainment, and the properties of a closed-cell stratocumulus cloud. *J. Adv. Model. Earth Syst.*, **9**, 2214–2229, https://doi.org/10.1002/2017MS001072.

Khairoutdinov, M., and Y. Kogan, 2000: A new cloud physics parameterization in a large-eddy simulation model of marine stratocumulus. *Mon. Wea. Rev.*, **128**, 229–243, https://doi.org/10.1175/1520-0493(2000)128<0229:ANCPPI>2.0.CO;2.

——, and D. A. Randall, 2003: Cloud resolving modeling of the ARM summer 1997 IOP: Model formulation, results, uncertainties, and sensitivities. *J. Atmos. Sci.*, **60**, 607–625, https://doi.org/10.1175/1520-0469(2003)060<0607:CRMOTA>2.0.CO;2.

Large, W. G., and S. Pond, 1982: Sensible and latent heat flux measurements over the ocean. *J. Phys. Oceanogr.*, **12**, 464–482, https://doi.org/10.1175/1520-0485(1982)012<0464:SALHFM>2.0.CO;2.

Leon, D. C., Z. Wang, and D. Liu, 2008: Climatology of drizzle in marine boundary layer clouds based on 1 year of data from CloudSat and Cloud-Aerosol Lidar and Infrared Pathfinder Satellite Observations (CALIPSO). *J. Geophys. Res.*, **113**, D00A14, https://doi.org/10.1029/2008JD009835.

Loeb, N. G., and Coauthors, 2018: Clouds and the Earth's Radiant Energy System (CERES) Energy Balanced and Filled (EBAF) top-of-atmosphere (TOA) Edition-4.0 data product. *J. Climate*, **31**, 895–918, https://doi.org/10.1175/JCLI-D-17-0208.1.

MacVean, M. K., and P. J. Mason, 1990: Cloud-top entrainment instability through small-scale mixing and its parameterization in numerical models. *J. Atmos. Sci.*, **47**, 1012–1030, https://doi.org/10.1175/1520-0469(1990)047<1012:CTEITS>2.0.CO;2.

McCoy, I. L., R. Wood, and J. K. Fletcher, 2017: Identifying meteorological controls on open and closed mesoscale cellular convection associated with marine cold air outbreaks. *J. Geophys. Res. Atmos.*, **122**, 11 678–11 702, https://doi.org/10.1002/2017JD027031.

McMichael, L. A., D. B. Mechem, S. Wang, Q. Wang, Y. L. Kogan, and J. Teixeira, 2019: Assessing the mechanisms governing the daytime evolution of marine stratocumulus using large-eddy simulation. *Quart. J. Roy. Meteor. Soc.*, **145**, 845–866, https://doi.org/10.1002/qj.3469.

Mellado, J.-P., C. S. Bretherton, B. Stevens, and M. C. Wyant, 2018: DNS and LES for simulating stratocumulus: Better together. *J. Adv. Model. Earth Syst.*, **10**, 1421–1438, https://doi.org/10.1029/2018MS001312.

Morton, B. R., G. I. Taylor, and J. S. Turner, 1956: Turbulent gravitational convection from maintained and instantaneous sources. *Proc. Roy. Soc. London*, **234A**, 1–23, https://doi.org/10.1098/rspa.1956.0011.

Pawlowska, H., J. L. Brenguier, and F. Burnet, 2000: Microphysical properties of stratocumulus clouds. *Atmos. Res.*, **55**, 15–33, https://doi.org/10.1016/S0169-8095(00)00054-5.

Rampal, N., and R. Davies, 2020: On the factors that determine boundary layer albedo. *J. Geophys. Res. Atmos.*, **125**, e2019JD032244, https://doi.org/10.1029/2019JD032244.

Sandu, I., and B. Stevens, 2011: On the factors modulating the stratocumulus to cumulus transitions. *J. Atmos. Sci.*, **68**, 1865–1881, https://doi.org/10.1175/2011JAS3614.1.

Savic-Jovcic, V., and B. Stevens, 2008: The structure and mesoscale organization of precipitating stratocumulus. *J. Atmos. Sci.*, **65**, 1587–1605, https://doi.org/10.1175/2007JAS2456.1.

Schneider, S. H., and R. E. Dickinson, 1976: Parameterization of fractional cloud amounts in climatic models: The importance of modeling multiple reflections. *J. Appl. Meteor.*, **15**, 1050–1056, https://doi.org/10.1175/1520-0450(1976)015<1050:POFCAI>2.0.CO;2.

Siebesma, A. P., and Coauthors, 2003: A large eddy simulation intercomparison study of shallow cumulus convection. *J. Atmos. Sci.*, **60**, 1201–1219, https://doi.org/10.1175/1520-0469(2003)60<1201:ALESIS>2.0.CO;2.

Stephens, G. L., 1978: Radiation profiles in extended water clouds. II: Parameterization schemes. *J. Atmos. Sci.*, **35**, 2123–2132, https://doi.org/10.1175/1520-0469(1978)035<2123:RPIEWC>2.0.CO;2.

Stevens, B., and G. Feingold, 2009: Untangling aerosol effects on clouds and precipitation in a buffered system. *Nature*, **461**, 607–613, https://doi.org/10.1038/nature08281.

——, and Coauthors, 2001: Simulations of trade wind cumuli under a strong inversion. *J. Atmos. Sci.*, **58**, 1870–1891, https://doi.org/10.1175/1520-0469(2001)058<1870:SOTWCU>2.0.CO;2.

Turton, J. D., and S. Nicholls, 1987: A study of the diurnal variation of stratocumulus using a multiple mixed layer model. *Quart. J. Roy. Meteor. Soc.*, **113**, 969–1009, https://doi.org/10.1002/qj.49711347712.

Twomey, S., 1974: Pollution and the planetary albedo. *Atmos. Environ.*, **8**, 1251–1256, https://doi.org/10.1016/0004-6981(74)90004-3.

——, 1977: The influence of pollution on the shortwave albedo of clouds. *J. Atmos. Sci.*, **34**, 1149–1152, https://doi.org/10.1175/1520-0469(1977)034<1149:TIOPOT>2.0.CO;2.

Wang, H., and G. Feingold, 2009: Modeling mesoscale cellular structures and drizzle in marine stratocumulus. Part II: The microphysics and dynamics of the boundary region between open and closed cells. *J. Atmos. Sci.*, **66**, 3257–3275, https://doi.org/10.1175/2009JAS3120.1.

Wood, R., 2012: Stratocumulus clouds. *Mon. Wea. Rev.*, **140**, 2373–2423, https://doi.org/10.1175/MWR-D-11-00121.1.

——, and C. S. Bretherton, 2006: On the relationship between stratiform low cloud cover and lower-tropospheric stability. *J. Climate*, **19**, 6425–6432, https://doi.org/10.1175/JCLI3988.1.

Yamaguchi, T., and D. A. Randall, 2008: Large-eddy simulation of evaporatively driven entrainment in cloud-topped mixed layers. *J. Atmos. Sci.*, **65**, 1481–1504, https://doi.org/10.1175/2007JAS2438.1.

——, and ——, 2012: Cooling of entrained parcels in a large-eddy simulation. *J. Atmos. Sci.*, **69**, 1118–1136, https://doi.org/10.1175/JAS-D-11-080.1.

——, G. Feingold, J. Kazil, and A. McComiskey, 2015: Stratocumulus to cumulus transition in the presence of elevated smoke layers. *Geophys. Res. Lett.*, **42**, 10 478–10 485, https://doi.org/10.1002/2015GL066544.

——, ——, and ——, 2017: Stratocumulus to cumulus transition by drizzle. *J. Adv. Model. Earth Syst.*, **9**, 2333–2349, https://doi.org/10.1002/2017MS001104.

Yanai, M., S. Esbensen, and J.-H. Chu, 1973: Determination of bulk properties of tropical cloud clusters from large-scale heat and moisture budgets. *J. Atmos. Sci.*, **30**, 611–627, https://doi.org/10.1175/1520-0469(1973)030<0611:DOBPOT>2.0.CO;2.